

Epitaxial Growth of CaMnO_{3-y} Films on LaAlO_3 (11 $\bar{2}$ 0) by Pulsed Direct Current Reactive Magnetron Sputtering

Erik Ekström, Anna Elsukova, Justine Grasland, Justinas Palisaitis, Ganpati Ramanath, Per O. Å Persson, Biplap Paul, Fredrik Eriksson, Arnaud le Febvrier, and Per Eklund*

CaMnO_3 is a perovskite with attractive magnetic and thermoelectric properties. CaMnO_3 films are usually grown by pulsed laser deposition or radio frequency magnetron sputtering from ceramic targets. Herein, epitaxial growth of CaMnO_{3-y} (002) films on a (11 $\bar{2}$ 0)-oriented LaAlO_3 substrate using pulsed direct current reactive magnetron sputtering is demonstrated, which is more suitable for industrial scale depositions. The CaMnO_{3-y} shows growth with a small in-plane tilt of $<\approx 0.2^\circ$ toward the (200) plane of CaMnO_{3-y} and the ($\bar{1}$ 104) with respect to the LaAlO_3 (11 $\bar{2}$ 0) substrate. X-ray photoelectron spectroscopy of the electronic core levels shows an oxygen deficiency described by $\text{CaMnO}_{2.58}$ that yields a lower Seebeck coefficient and a higher electrical resistivity when compared to stoichiometric CaMnO_3 . The LaAlO_3 (11 $\bar{2}$ 0) substrate promotes tensile-strained growth of single crystals. Scanning transmission electron microscopy and electron energy loss spectroscopy reveal antiphase boundaries composed of Ca on Mn sites along $<101>$ and $<002>$, forming stacking faults.

1. Introduction

Perovskite CaMnO_3 has attractive magnetic, catalytic, and thermoelectric properties, and a Pnma-to-Pm $\bar{3}$ m phase transition at $\approx 900^\circ\text{C}$.^[1–4] The choice of substrate is important for epitaxial growth of CaMnO_3 films because the first few layers determine the film structure, quality, and properties.^[5] Perovskite-structured crystals, e.g., LaAlO_3 and SrTiO_3 , are commonly used as substrates for growing CaMnO_3 films because of better lattice matching than hexagonal-structured substrates (e.g., sapphire^[6–8]). For CaMnO_3 films grown on LaAlO_3 , the stress can influence the magnetic properties of the film.^[7] LaAlO_3 is specified by the R $\bar{3}$ c space group, but it is more commonly referred to a pseudocubic lattice specified by Pm $\bar{3}$ m space


group with lattice parameter $a = 3.81 \text{ \AA}$; thus, LaAlO_3 (01 $\bar{1}$ 2) is also referred to as LaAlO_3 (001). A similar simplification for CaMnO_3 yields a lattice parameter of $a = 3.72 \text{ \AA}$.

Growing CaMnO_3 by direct current (DC) sputter deposition usually results in heavy arcing due to metal target poisoning with oxygen. This problem is diminished significantly when the films are deposited by radio frequency (RF) magnetron sputtering or pulsed laser deposition (PLD).^[9] However, these techniques are not easily scalable for industrial applications. Here, we grow epitaxial CaMnO_3 thin films on LaAlO_3 (11 $\bar{2}$ 0)-oriented substrates, i.e., using a different substrate orientation than commonly used, by pulsed DC reactive magnetron sputtering. This method is faster and more readily scalable than PLD or RF magnetron sputtering.^[10] The CaMnO_3 films are oxygen-deficient and grow with a small in-plane tilt of $<\approx 0.2^\circ$ toward the (200) planes in the film and ($\bar{1}$ 104) planes in LaAlO_3 . Scanning transmission electron microscopy (STEM) and electron energy loss spectroscopy (EELS) confirm high-quality films with dark contours along $<101>$ and $<002>$ arising from stacking faults with defects composed of Ca occupying Mn sites. The films exhibit room-temperature Seebeck coefficient and resistivity of $-200 \mu\text{V K}^{-1}$ and $4 \Omega \text{ cm}$, respectively, both of which are comparable to reported values for oxygen-deficient CaMnO_{3-y} films. The epitaxial CaMnO_3 films on LaAlO_3 (11 $\bar{2}$ 0) contrast to the multidomain epitaxy seen in films on LaAlO_3 (01 $\bar{1}$ 2) and may result in decreased charge-carrier scattering.

E. Ekström, A. Elsukova, J. Palisaitis, P. O. Å. Persson, B. Paul, F. Eriksson, A. Febvrier, P. Eklund
Thin Film Physics Division
Department of Physics, Chemistry and Biology (IFM)
Linköping University
SE-581 83 Linköping, Sweden
E-mail: per.eklund@liu.se

J. Grasland
CNRS
CEA
INSA CVL
GREMAN UMR 7347
IUT de Blois Université François Rabelais de Tours
15 rue de la chocolaterie, CS 2903, 41029 Blois Cedex, France

G. Ramanath
Materials Science and Engineering Department
Rensselaer Polytechnic Institute
Troy, NY 12180, USA

 The ORCID identification number(s) for the author(s) of this article can be found under <https://doi.org/10.1002/pssr.202100504>.

© 2022 The Authors. physica status solidi (RRL) Rapid Research Letters published by Wiley-VCH GmbH. This is an open access article under the terms of the Creative Commons Attribution License, which permits use, distribution and reproduction in any medium, provided the original work is properly cited.

DOI: 10.1002/pssr.202100504

2. Experimental Section

CaMnO_{3-y} films were grown by pulsed reactive magnetron sputtering of elemental 99.9% purity Ca and Mn targets (Plasmaterials, Livermore, CA, USA) on $10 \times 10 \text{ mm}^2$ LaAlO_3 (11 $\bar{2}0$) substrates at 600°C in an ultrahigh vacuum system with a base pressure of 10^{-6} Pa (10^{-8} mbar) described in detail elsewhere.^[11] The LaAlO_3 substrates were cleaned by successively immersing in Hellmanex for 3 min and in deionized water for 2 min. This process was repeated once, followed by ultrasonic cleaning in acetone and ethanol for 10 min each, and blow-drying with N_2 gas. The Ca and Mn magnetrons were operated at 75 and 45 W, respectively, using a 50 kHz pulsing frequency and an on time of 2 μs . The reverse voltage and crowbar delay were set to 10% and 30 μs , respectively. CaMnO_{3-y} deposition was carried out at 0.46 Pa (3.5 mTorr) using 1:20 oxygen/argon mixture with 3 sccm oxygen and 60 sccm Ar for 240 min to obtain a 73 nm-thick film.

Core-level spectra were obtained by X-ray photoelectron spectroscopy (XPS) using a Kratos Axis Ultra DLD instrument with a monochromatic Al K α radiation source ($h\nu = 1486.6 \text{ eV}$) with the anode power set to 150 W and a $1.1 \times 10^{-9} \text{ Torr}$ ($1.5 \times 10^{-7} \text{ Pa}$) base pressure. A $3 \times 3 \text{ mm}^2$ raster area was obtained by sputter cleaning the sample surface with a 0.5 keV Ar^+ beam incident onto the sample surface at a 20° angle, and the spectra were collected from a $0.3 \times 0.7 \text{ mm}^2$ area at normal emission angle. A low-energy electron gun operated at filament current 1.83 A, charge balance 2.06 V, and filament bias 1 V was used to compensate sample charging effects. The analyzer pass energy was set to 20 eV, yielding a 0.55 eV full width at half maximum for the Ag $3d_{5/2}$ peak. The KolXPD software^[12] was used to fit the peaks using the pseudo-Voigt function (70% Gaussian, 30% Lorentzian) formalism after a Shirley background subtraction. The spin-orbit splitting intensity ratios were fixed at $\frac{1}{2}$ for the Ca $2p_{3/2}$ and Ca $2p_{1/2}$ core levels separated by 3.5 eV.

For cross-sectional transmission electron microscopy (TEM) analysis, the sample was cut along two in-plane directions $[\bar{1}104]$ and $[1\bar{1}02]$ into $0.6 \times 1.8 \text{ mm}^2$ pieces and glued to a Ti grid using araldite. The Ti grid was mechanically thinned down to $\approx 50 \mu\text{m}$ using diamond polishing papers. The samples were ion milled in a Gatan's Precision Ion Polishing system to create electron-transparent regions using 5 keV Ar^+ ions incident on to the surface at 5° and a follow-up polishing by a 2 keV Ar^+ beam.

The film microstructure was probed using high-angle annular dark field (HAADF) STEM imaging, selective area electron diffraction (SAED), and EELS. Characterization was performed using the Linköping double C_s -corrected FEI Titan³ 60-300, operated at 300 kV. We obtained sub-Ångström resolution in HAADF-HRSTEM images using a 21.5 mrad convergence semi-angle with $\approx 60 \text{ pA}$ probe beam current and an angular detection range of 46–200 mrad. STEM-EELS spectrum images of 32×32 pixels were acquired for 1 min using a 0.25 eV/channel energy dispersion, 0.2 s pixel dwell time, and a collection semiangle of 55 mrad of the employed Gatan GIF Quantum ERS postcolumn imaging filter. Elemental Ca and Mn distribution maps were extracted from EELS spectrum images by background subtraction, using a power law, and choosing characteristic edges Ti-L₂₃ (340–280 eV) and Mn-L₂₃ (640–490 eV) energy loss integration windows.

The X-ray diffractometry (XRD) and X-ray reflectivity (XRR) were carried out in a PANalytical Empyrean diffractometer equipped with a copper Cu K α ($\lambda = 1.54 \text{ Å}$) source operated at 45 kV and 40 mA, a hybrid mirror on the incidence beam path, and a triple-axis Ge 220 analyzer on the diffracted beam path, and a PIXcel3D detector operated in open detection mode. The XRR data were fitted using the X'Pert Reflectivity program. Scanning electron microscopy (SEM) was carried out using a LEO Gemini 1550 Zeiss instrument operated at 3 kV using an in-lens secondary electron detector.

The Seebeck coefficient α was measured in a home-built setup, previously described,^[13] equipped with two Peltier heat sources and two 0.1 mm-diameter K-type thermocouples, for creating a temperature gradient and for measuring the temperature, respectively. Two, $1.5 \times 4 \text{ cm}^2$ in size, Cu electrodes were attached to, but electrically isolated from, the thermocouples, in contact with the hot and cold spots, and connected to a Keithley 2001 multimeter. The electrical resistivity was determined from four-point-probe sheet resistance measurements using a Jandel RM3000 probe and the film thickness, as determined by XRR measurements, shown in the Supporting Information.

3. Results and Discussion

Fitting XRR data from as-deposited CaMnO_3 (see Figure S1, Supporting Information) showed a film thickness of 73 nm with a 4.28 g cm^{-3} density and a 2.7 nm surface roughness. The estimated film density is $\approx 7\%$ lower than the theoretical value^[14] of 4.59 g cm^{-3} . SEM micrographs (see Figure S2, Supporting Information) show a film surface with small linear voids, consistent with the estimated surface roughness. X-ray diffractograms (Figure S3, Supporting Information) show two sets of peaks that are also seen from a bare substrate (inset in Figure S3, Supporting Information), i.e., all observed peaks are from the substrate.

Cross-sectional HAADF-STEM images (Figure 1) show a film thickness of $\approx 70 \text{ nm}$ thick, corroborating the XRR analysis. The

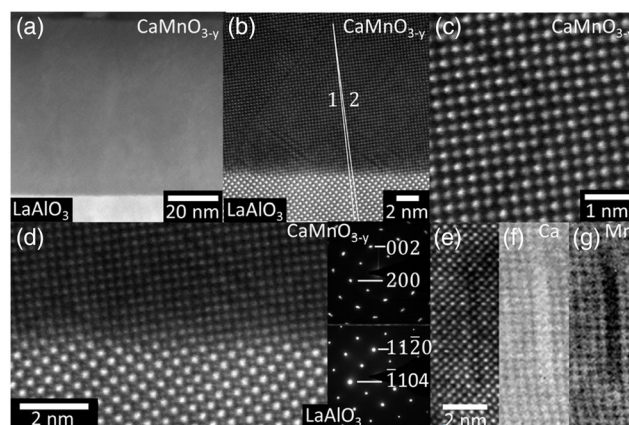


Figure 1. HAADF-STEM images of the film are shown in (a–d) at different magnification. SAED patterns for the film (top pattern) and substrate (bottom pattern) are shown as insets in (d). A STEM image of a dark line is shown in (e) and corresponding EELS maps for Ca and Mg are shown in (f,g), respectively. The white lines in (b) are drawn along the film lattice (left line) and substrate lattice (right line) to visualize the small angle difference.

homogeneous contrast indicates no apparent grain boundaries in the low magnification images (Figure 1a); however, dark lines appear throughout the entire film. The film is grown with a small angular offset ($\approx 0.2^\circ$) with respect to the substrate, as indicated by the superimposed lines drawn across the film–substrate interface marked 1 (following the film lattice) and 2 (following the substrate lattice) in Figure 1b. This offset between film and substrate crystal structure is further verified by SAED patterns as small radial smear of the film and the substrate patterns (insets in Figure 1d), additional STEM analysis (see Figure S4, Supporting Information). The film–substrate interface is sharp (Figure 1d) with no apparent defects, suggesting that the film is of high epitaxial quality.

Based on the SAED patterns, we can describe the crystallographic relationship between the film and the substrate as CaMnO_{3-y} (002) // LaAlO_3 (11 $\bar{2}$ 0) and CaMnO_{3-y} (200) // LaAlO_3 ($\bar{1}$ 104). Furthermore, correlations between plan-view images of the film and the SAED patterns (see Figure S5, Supporting Information) indicate that the dark lines follow the $\langle 101 \rangle$ directions in the CaMnO_{3-y} film. We observed only one domain of the CaMnO_3 films on LaAlO_3 (11 $\bar{2}$ 0), in contrast to three different orientations reported^[7] for CaMnO_3 films grown on (01 $\bar{1}$ 2)-oriented LaAlO_3 substrate.

Examples of the dark lines are shown in (Figure 1b-d). The applied mass contrast imaging conditions yield that these lines are associated with a locally lower atomic number. In addition, we observe an extended bond length across the lines ($\approx 14\%$). EELS elemental maps of the dark lines (Figure 1f-g) reveal a significantly higher Ca signal and a lower Mn signal that indicate agglomeration of defects on specific planes, where Ca substitutes for Mn. Consequently, the comparatively longer Ca–O bonds also expand the lattice.

Figure 2 shows the corresponding analysis of a sample prepared with a 90° in-plane rotation that shows similar results, but with some notable differences. The dark lines appear in the $\langle 002 \rangle$ growth direction, and some of the lines span the entire film thickness (see Figure 2a). Also, in this projection

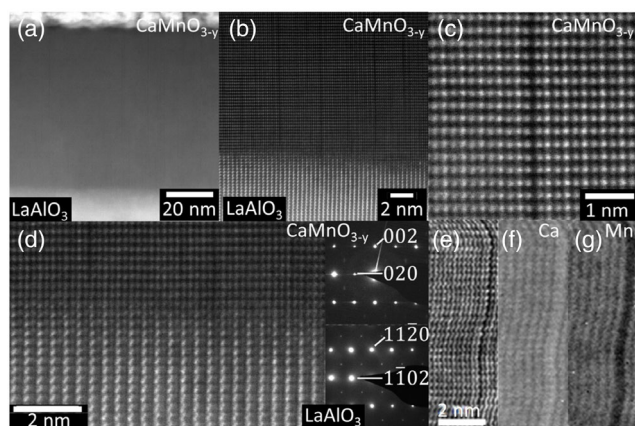


Figure 2. HAADF-STEM images of the film is shown in (a–d) at different resolution. SAED patterns for the film (top pattern) and substrate (bottom pattern) are shown as insets in (d). A STEM image of a dark line is shown in (e) and associated EELS maps are shown in (f,g) corresponding to Ca signal and Mn signal, respectively.

the lines correlate to defects and a locally increased bond length (Figure 2b-c). The width of the dark lines is approximately 33% larger in relation to the ambient lattice and is much larger than for the dark lines in Figure 1. The SAED pattern (Figure 2d inset) confirms the epitaxial relationship described above (Figure 1). The defects are correlated with the formation of anti-phase boundaries, which has been reported as a relaxation mechanism in perovskites^[15] and other structures.^[16]

Following the off angle tilt growth found in STEM, an additional XRD measurement was performed as shown in Figure 3 where two different measurements on the same film were performed. The difference between the two measurements is the tilt in ω (incidence angle) and χ (tilt angle). ω and χ are aligned on the substrate peak for the red curve and aligned on the film on the blue curve. As clearly seen, the 002 film peak of CaMnO_3 is observed for the tilted alignment, matching the tilt observed in STEM. It is apparent that the film peak is hidden beneath the substrate peak if not properly aligned on. Additionally, the intensity scale difference between the red (substrate) and blue (film) curve is on the order of 100 where the red curve has higher intensity.

Rocking curves on the substrate (b) and film (c) are obtained at the alignment on respective material. The full width at half maximum of the two rocking curves is similar, implying that the crystal quality of the film and substrate is similar.

XPS was used to obtain compositional and bonding information. The Ca 2p, Mn 3s, and O 1s core level peaks are shown in Figure 4. The XPS analyses showed an overall composition of

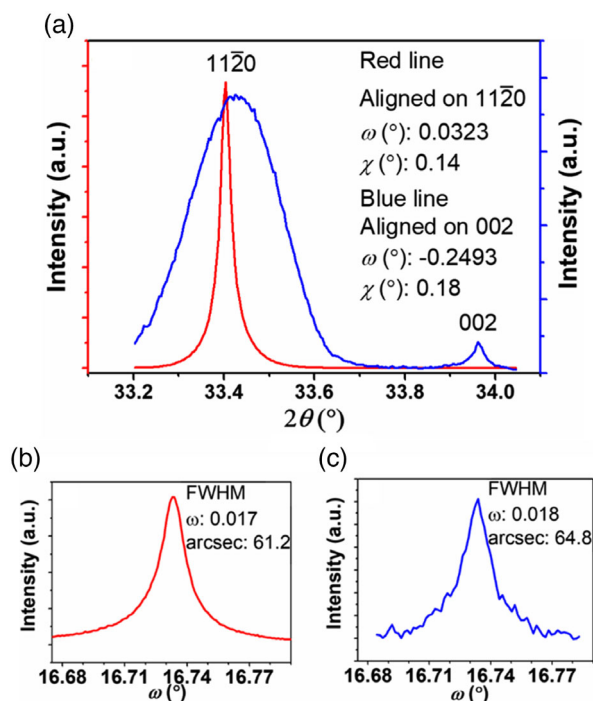


Figure 3. The two X-ray diffractograms shown in (a) represent two different alignments of the diffractometer. The red curve represents alignment on the substrate peak and the blue curve represents alignment on the film peak. Parts (b) and (c) are rocking curves performed on the substrate and film, respectively.

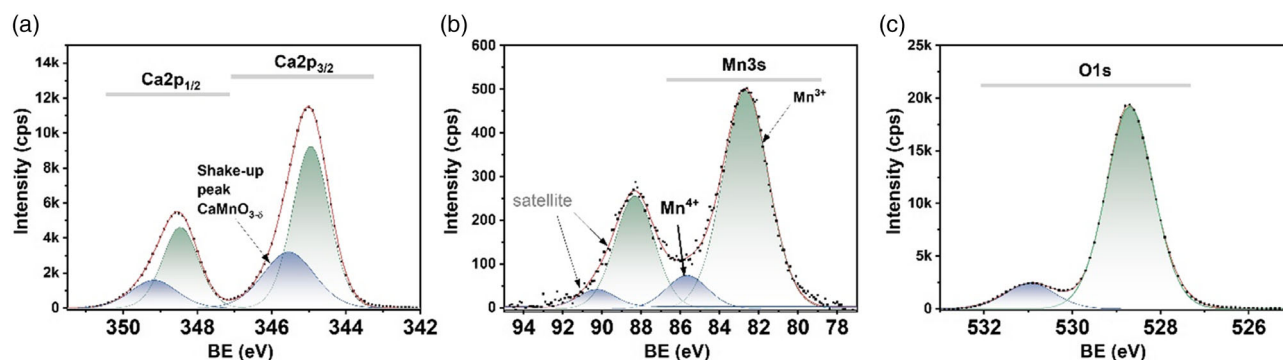


Figure 4. The XPS data (black dots) and fit (solid curves) in the vicinity of a) Ca 2p, b) Mn 3s, and c) O 1s core level bands from CaMnO_{3-y} films.

$\text{CaMnO}_{2.58}$. TEM-EDX was performed, showing a substoichiometric composition of $\text{CaMnO}_{2.65}$, supporting the composition determined by XPS as well as the low film density determined by XRR. Peak fits show that the Ca 2p bands consist of Ca 2p_{3/2} and 2p_{1/2} subbands at ≈ 345.0 eV (FWHM = 1.09 eV) and 348.5 eV (FWHM = 1.05 eV) and shake-up peaks at 345.6 eV (FWHM = 1.29 eV) and 349.2 eV (FWHM = 1.25 eV) (see Figure 4a) that are indicative of a higher oxidation state, suggesting the presence of oxygen vacancies. The two Mn 3s core level peaks (Figure 4b) correspond to Mn^{3+} and Mn^{4+} at 82.7 eV (FWHM = 2.75 eV) and 85.7 eV (FWHM = 2.50 eV), respectively, and their satellite peaks at 5.6 and 4.7 eV, respectively, indicating manganese oxides^[17–19] also indicate oxygen vacancies^[18,19] that induce decrease in the Mn oxidation number from +4 to +3. The O 1s peak (Figure 4c) consists of two core level subbands at 528.7 eV (FWHM = 1.26 eV) from the oxygen in the bulk material and 530.9 eV (FWHM = 1.31 eV), corresponding to oxygen in the bulk and the surface, respectively. Oxygen vacancies are known to form in CaMnO_3 by the reduction of Mn^{3+} ions from Mn^{4+} ions.^[20] Thus, it is unlikely that the observed Mn^{3+} would be an artifact of sputter cleaning prior to XPS. This inference is supported by the fact that the compositions obtained from both EDX and XPS indicate Mn^{3+} content than Mn^{4+} .

These results indicate that the LaAlO_3 (11 $\bar{2}$ 0) substrates support the epitaxial growth of substoichiometric CaMnO_{3-y} films. The film growth is likely strained to enable lattice matching with the substrate. A possible explanation for the low oxygen content is that the formation energy of oxygen vacancies is decreased when CaMnO_3 is under tensile stress and the film relaxes by the so-called chemical strain relaxation.^[7,19,21,22] The oxygen vacancies can also form due to insufficient oxygen supply during growth,^[20] which could be improved by increasing the oxygen flow during the synthesis process or through a postannealing step.

The room-temperature Seebeck coefficient, α , and electrical resistivity, ρ , were determined to be $\alpha = -208 \mu\text{V K}^{-1}$ and $\rho = 4 \Omega \text{ cm}$, respectively. These values are lower than that reported^[23] for stoichiometric CaMnO_3 , namely, $-300 \mu\text{V K}^{-1} \leq \alpha < -400 \mu\text{V K}^{-1}$ and $1 \Omega \text{ cm} \leq \rho \leq 10 \Omega \text{ cm}$, but are comparable to values in oxygen-deficient CaMnO_3 films. First-principle calculations^[24] by Molinari et al. indicate $-200 \mu\text{V K}^{-1} \leq \alpha < -220 \mu\text{V K}^{-1}$ and $2\text{--}3 \Omega \text{ cm}$ for $\text{CaMnO}_{2.5}$. The lower Seebeck coefficient in substoichiometric CaMnO_3 can be explained by oxygen vacancy-induced decreased gradients in the density of states near the conduction band bottom.^[23–27]

4. Conclusions

In summary, this study has shown that epitaxial CaMnO_{3-y} films can be grown on LaAlO_3 (11 $\bar{2}$ 0) substrates by pulsed DC magnetron sputtering. A well-defined single-crystal structure with occasional stacking faults where Ca ions occupy Mn ion sites was observed. STEM and EELS reveal antiphase boundaries composed of Ca on Mn sites along $\langle 101 \rangle$ and $\langle 002 \rangle$. XPS and EDS revealed a substoichiometric composition of around $\text{CaMnO}_{2.60}$, likely due to oxygen vacancies. The Seebeck coefficient of $-208 \mu\text{V K}^{-1}$ and the electrical resistivity of $4 \Omega \text{ cm}$ are consistent with other substoichiometric CaMnO_3 films. The LaAlO_3 (11 $\bar{2}$ 0) substrate promotes tensile-strained growth of single crystals.

Supporting Information

Supporting Information is available from the Wiley Online Library or from the author.

Acknowledgements

The authors thank Babak Bakhit for performing the XPS measurements. The authors acknowledge funding the Swedish Research Council (VR) under project no. 2016-03365, the Knut and Alice Wallenberg Foundation through the Wallenberg Academy Fellows program (grant no. KAW 2020.0196) and through support of the Electron Microscopy Laboratory at Linköping University, the Swedish Government Strategic Research Area in Materials Science on Functional Materials at Linköping University (Faculty Grant SFO-Mat-LiU No. 2009 00971), and the Swedish Energy Agency under project 46519-1. P.O.Å.P. also acknowledges the Swedish Foundation for Strategic Research (SSF) through the Research Infrastructure Fellow program no. RIF 14-0074.

Conflict of Interest

The authors declare no conflict of interest.

Data Availability Statement

The data that support the findings of this study are available from the corresponding author upon reasonable request.

Keywords

CaMnO₃, epitaxy, perovskites, PVD

Received: September 29, 2021

Revised: December 20, 2021

Published online:

- [1] H. Taguchi, M. Nagao, T. Sato, M. Shimada, *J. Solid State Chem.* **1989**, 78, 312.
- [2] K. Koumoto, R. Funahashi, E. Guilmeau, Y. Miyazaki, A. Weidenkaff, Y. Wang, C. Wan, X.-D. Zhou, *J. Am. Ceram. Soc.* **2013**, 96, 1.
- [3] J. Klarbring, S. I. Simak, *Phys. Rev. B* **2018**, 97, 024108.
- [4] K. Zhang, X. Han, Z. Hu, X. Zhang, Z. Tao, J. Chen, *Chem. Soc. Rev.* **2015**, 44, 699.
- [5] J. A. Venables, G. D. T. Spiller, M. Hanbucken, *Rep. Progr. Phys.* **1984**, 47, 399.
- [6] H.-J. Kim, T. K. Chau, V.-H. Nguyen, *New Phys. SAE Mulli.* **2017**, 67, 679.
- [7] T. Günter, E. Bousquet, A. David, Ph. Boullay, Ph. Ghosez, W. Prellier, M. Fiebig, *Phys. Rev. B* **2012**, 85, 214120.
- [8] C. L. Flint, A. J. Grutter, C. A. Jenkins, E. Arenholz, Y. Suzuki, *J. Appl. Phys.* **2014**, 115, 17D712.
- [9] W. D. Sproul, D. J. Christie, D. C. Carter, *Thin Solid Films* **2005**, 491, 1.
- [10] J. Sellers, *Surf. Coat. Technol.* **1998**, 98, 1245.
- [11] D. H. Trinh, M. Ottosson, M. Collin, I. Reineck, L. Hultman, H. Högberg, *Thin Solid Films* **2008**, 516, 4977.
- [12] J. Libra, KolXPD: Spectroscopy Data Measurement and Processing.
- [13] B. Xin, A. Le Febvrier, L. Wang, N. Solin, B. Paul, P. Eklund, *Mater. Des.* **2021**, 210, 110033.
- [14] *Springer Materials*, Springer-Verlag, Berlin Heidelberg and Material Phases Data System (MPDS), Switzerland and National Institute for Materials Science (NIMS), Japan. https://materials.springer.com/isp/crystallographic/docs/sd_1403122.
- [15] Y. Q. Wang, W. S. Liang, P. K. Petrov, N. M. Alford, *Appl. Phys. Lett.* **2011**, 98, 091910.
- [16] M. Luysberg, R. G. S. Sofin, S. K. Arora, I. V. Shvets, *Phys. Rev. B* **2009**, 80, 024111.
- [17] F. Muller, R. de Masi, D. Reinicke, P. Steiner, S. Hüfner, K. Stöwe, *Surf. Sci.* **2002**, 520, 158.
- [18] J. Du, T. Zhang, F. Cheng, W. Chu, Z. Wu, J. Chen, *Inorg. Chem.* **2014**, 53, 9106.
- [19] R. U. Chandrasena, W. Yang, Q. Lei, M. U. Delgado-Jaime, K. D. Wijesekara, M. Golalikhani, B. A. Davidson, E. Arenholz, K. Kobayashi, M. Kobata, F. M. F. de Groot, U. Aschauer, N. A. Spaldin, X. Xi, A. X. Gray, *Nano Lett.* **2017**, 17, 794.
- [20] Z. Zeng, M. Greenblatt, M. Croft, *Phys. Rev. B* **1999**, 59, 8784.
- [21] U. Aschauer, R. Pfenninger, S. M. Selbach, T. Grande, N. A. Spaldin, *Phys. Rev. B* **2013**, 88, 054111.
- [22] T. Grande, J. R. Tolchard, S. M. Selbach, *Chem. Mater.* **2012**, 24, 338.
- [23] Y. N. Feng, X. Jiang, E. Ghafari, B. Kucukgok, C. Zhang, I. Ferguson, N. Lu, *Adv. Composit. Hybrid Mater.* **2018**, 1, 114.
- [24] M. Molinari, D. A. Tompsett, S. C. Parker, F. Azough, R. Freer, *J. Mater. Chem.* **2014**, A 2, 14109.
- [25] V. Tayari, B. V. Senkovskiy, D. Rybkovskiy, N. Ehlen, A. Fedorov, C.-Y. Chen, J. Avila, M. Asensio, A. Perucchi, P. di Pietro, L. Yashina, I. Fakhri, N. Hemsworth, M. Petrescu, G. Gervais, A. Grüneis, T. Szkopek, *Phys. Rev. B* **2018**, 97, 9.
- [26] J. P. Heremans, V. Jovovic, E. S. Toberer, A. Saramat, K. Kurosaki, A. Charoenphakdee, S. Yamanaka, G. J. Snyder, *Science* **2008**, 321, 554.
- [27] C. S. Huang, H. Fang, Z. H. Xu, X. Zheng, X. X. Ruan, *Results Phys.* **2019**, 13, 102337.